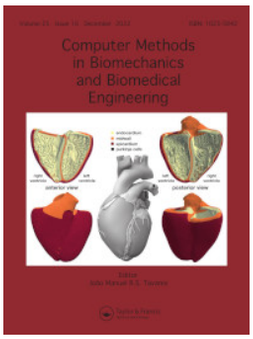

Taylor & Francis
Taylor & Francis Group

Computer Methods in Biomechanics and Biomedical Engineering

ISSN: (Print) (Online) Journal homepage: https://www.tandfonline.com/loi/gcmb20

# A peridynamic formulation for nonlocal bone remodelling

E. Schaller, A. Javili, I. Schmidt, A. Papastavrou & P. Steinmann

**To cite this article:** E. Schaller, A. Javili, I. Schmidt, A. Papastavrou & P. Steinmann (2022) A peridynamic formulation for nonlocal bone remodelling, Computer Methods in Biomechanics and Biomedical Engineering, 25:16, 1835-1851, DOI: 10.1080/10255842.2022.2039641

**To link to this article:** https://doi.org/10.1080/10255842.2022.2039641

COMPUTER METHODS IN BIOMECHANICS AND BIOMEDICAL ENGINEERING
2022, VOL. 25, NO. 16, 1835–1851
https://doi.org/10.1080/10255842.2022.2039641



# A peridynamic formulation for nonlocal bone remodelling

E. Schaller[a], A. Javili[b], I. Schmidt[c], A. Papastavrou[c] and P. Steinmann[a]

[a]Institute of Applied Mechanics, Friedrich-Alexander-Universität Erlangen-Nürnberg, Erlangen, Germany; [b]Department of Mechanical Engineering, Bilkent University, Ankara, Turkey; [c]Faculty of Mechanical Engineering, Nuremberg Tech, Nuremberg, Germany

**ABSTRACT**

Bone remodelling is a complex biomechanical process, which has been studied widely based on the restrictions of local continuum theory. To provide a nonlocal bone remodelling framework, we propose, for the first time, a peridynamic formulation on the macroscale. We illustrate our implementation with a common benchmark test as well as two load cases of the proximal femur. On the one hand, results of our peridynamic model with diminishing nonlocality measure converge to the results of a local finite element model. On the other hand, increasing the neighbourhood size shows to what extent the additional degree of freedom, the nonlocality, can influence the density evolution.

**ARTICLE HISTORY**
Received 13 July 2021
Accepted 4 February 2022

**KEYWORDS**
Bone remodelling; peridynamics; nonlocal material; density evolution; influence of nonlocality

## 1. Introduction

Bone remodelling is a continuously ongoing mechanism of bone tissue to adapt its external and mainly internal trabecular bone structure to mechanical and biological alterations. In this process, the interaction of various cell types (osteoblasts, osteoclasts and osteocytes) plays a crucial role for bone formation and resorption. Wolff (1892) postulated Wolff's law of bone remodelling to describe the functional adaption of living material to external mechanical stimulus. Cowin and Hegedus (1976) set the stage for mathematically describing the coupling of bone evolution and mechanical stimulus with the first continuum model for bone remodelling.

The complex process of bone remodelling remains an ongoing modelling challenge, as outlined by an extensive literature review of Della Corte et al. (2020), where different aspects of bone remodelling are addressed. In this regard, the nature of the biological stimulus that mainly controls the bone density evolution is one of the research focuses. George et al. (2018) proposed a multiphysics stimulus dependent on mechanical, molecular and cellular stimuli. In order to capture the nonlocal cell to cell communication of bone sensor cells via a mechanosensory network (Martin et al. 1998), Kumar et al. (2011) focused on a nonlocal stimulus that implies spatial averaging, whereas Giorgio et al. (2019) incorporated a diffusive stimulus emerging from osteocytes. Considering the attractor stimulus that determines homeostasis, Papastavrou, Schmidt, Deng et al. (2020) examined a non-constant and age-dependent attractor stimulus.

Despite the already established nonlocal biological stimulus of Kumar et al. (2011), the governing equations for the mechanical evolution equations have been defined only in a local continuum form. Nonlocal continuum theories, such as peridynamics (PD) introduced by Silling (2000), can be used to capture and study nonlocal material behaviour. In contrast to classical continuum mechanics (CCM), the material behaviour at every continuum point in the peridynamic theory is affected by its finite-size neighbourhood. Thus, the governing equations are obtained in integrodifferential form based on the force density resulting from interaction of continuum points (Silling 2000).

PD was initially established to overcome singularities appearing in fracture mechanics. In recent years, the application of PD has expanded significantly, as extensively reviewed by Javili et al. (2019). In the biomechanical field, PD was already utilised for bone modelling, while retaining the original intention for predicting crack formation. Deng et al. (2009) studied microcrack propagation and healing processes in cortical bone using a nonlocal multi-scale field theory and Ghajari et al. (2014) introduced a peridynamic material model to analyse dynamic crack propagation in orthotropic media like cortical bone.

CONTACT E. Schaller emely.schaller@fau.de

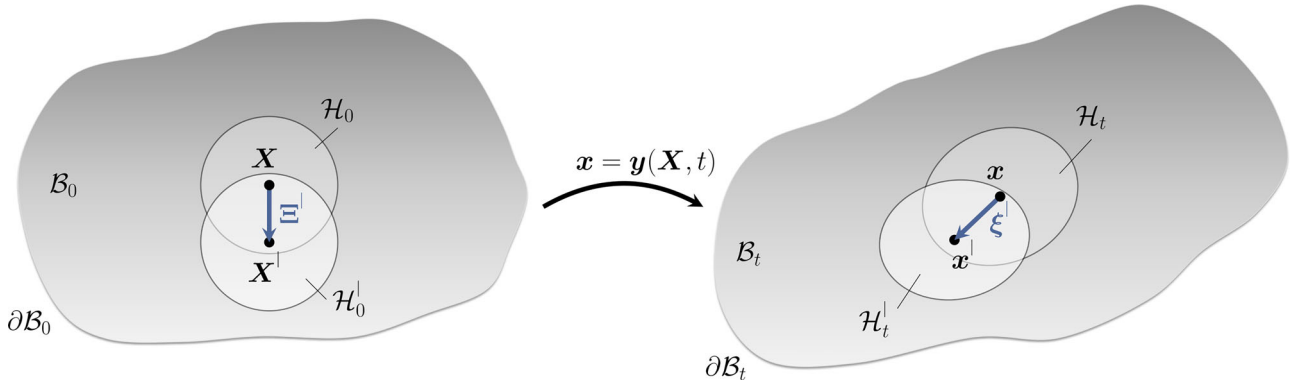


**Figure 1.** A continuum body in its material configuration $\mathcal{B}_0 \subset \mathbb{R}^3$ is mapped to its spatial configuration $\mathcal{B}_t \subset \mathbb{R}^3$ via the nonlinear deformation map $\boldsymbol{y}$.

To the authors' knowledge, the nonlocal material behaviour of bone tissue regarding the remodelling process has not been studied yet. Motivated by the lack of a fully nonlocal material model, the objective of this paper is to introduce a peridynamic formulation for bone remodelling at the macroscale for the first time by extending the local nonlinear evolution equations of Kuhl and Steinmann (2003) in a peridynamic sense.

The paper is organised as follows. In Section 2, we introduce the peridynamic equations for bone remodelling with the governing balance and constitutive equations. Section 3 briefly outlines the computational implementation. Subsequently, in Section 4, we demonstrate the characteristics of our peridynamic formulation with two numerical examples. First, we perform a simple uniaxial benchmark test to validate our nonlocal formulation. In a second numerical example, we focus on the density distribution evolving throughout the proximal femur. Here, we additionally examine the influence of the prescribed boundary conditions by comparing two load cases. The conclusion in Section 5 summarises the main findings of the paper and provides further outlook.

## 2. Problem definition

In the following, we model bone as a continuum domain assuming that bone tissue is continuously distributed at the macro scale. We use the continuum-kinematics-inspired peridynamic (CPD) formulation of Javili et al. (2019) with only one-neighbour interactions, which is equivalent to bond-based PD in the framework of Silling (2000), and develop a nonlocal formulation for bone remodelling. Thereby, we extend the nonlinear equations for open systems as proposed for local CCM, presented in Kuhl et al. (2003), Kuhl and Steinmann (2003), and Papastavrou, Schmidt, Deng et al. (2020), to their nonlocal counterparts within a PD formulation.

### 2.1. Kinematics

In accordance with the classical continuum theory, we consider a continuum body in its material configuration $\mathcal{B}_0 \subset \mathbb{R}^3$ at time $t_0 \subset \mathbb{R}_+$ and in its spatial configuration $\mathcal{B}_t \subset \mathbb{R}^3$ at $t > t_0 \subset \mathbb{R}_+$ as illustrated in Figure 1. The boundary is denoted by $\partial\mathcal{B}_0$ and $\partial\mathcal{B}_t$, respectively. The material coordinates $\boldsymbol{X}$ of the continuum points are mapped via the nonlinear deformation map $\boldsymbol{y}$ to their spatial coordinates $\boldsymbol{x}$ as

$$\boldsymbol{x} = \boldsymbol{y}(\boldsymbol{X}, t): \quad \mathcal{B}_0 \times \mathbb{R}_+ \to \mathcal{B}_t. \tag{1}$$

In PD theory, every continuum point interacts with continuum points in its finite neighbourhood, the so called horizon $\mathcal{H}_0$ that is typically a spherical neighbourhood of $\boldsymbol{X}$ defined by the radius $\delta$ in the material configuration. The horizon $\mathcal{H}_0$ is mapped to its spatial configuration $\mathcal{H}_t$ as

$$\mathcal{H}_t = \boldsymbol{y}(\mathcal{H}_0). \tag{2}$$

The horizon size $\delta$ has an influence on the nonlocal material behaviour at $\boldsymbol{X}$ and is consequently considered a material parameter of PD. Note that the local continuum theory is recovered by a vanishing horizon size.

Quantities of neighbours within $\mathcal{H}_0$ are marked with a superscript line $\{\bullet\}'$. The position vector in the material configuration $\boldsymbol{X}' \in \mathcal{H}_0$ is mapped via the nonlinear deformation map $\boldsymbol{y}$ to the position vector $\boldsymbol{x}' \in \mathcal{H}_t$ in the spatial configuration. The line vectors between the continuum point and any of its neighbours are defined by

$$\boldsymbol{\Xi}' := \boldsymbol{X}' - \boldsymbol{X} \qquad \text{and} \qquad \boldsymbol{\xi}' := \boldsymbol{x}' - \boldsymbol{x}, \tag{3}$$

in the material and spatial configurations, respectively.

In the following, we derive the governing equations in the material configuration. Therein, the material time

**Table 1.** Comparison of governing equations in the peridynamic and classic continuum formulation.

| | PD | CCM |
|---|---|---|
| balance of mass | $\mathrm{D}_t\rho_0 = \mathcal{R}_0$ | $\mathrm{D}_t\rho_0 = \mathcal{R}_0$ |
| balance of linear momentum | $\int_{\mathcal{H}_0} \boldsymbol{p}^{\shortmid}\,\mathrm{d}V^{\shortmid} = \boldsymbol{0}$ | $\mathrm{Div}\mathbf{P} = \boldsymbol{0}$ |
| governing quantity | $\boldsymbol{p}^{\shortmid} := \frac{\partial \psi_0^{\shortmid}}{\partial \boldsymbol{\xi}^{\shortmid}}$ | $\mathbf{P} := \frac{\partial \Psi_0}{\partial \mathbf{F}}$ |
| volume-specific energy density | $\Psi_0 = \frac{1}{2}\int_{\mathcal{H}_0} \left[\frac{\rho_0^{\shortmid}}{\rho_0^*}\right]^n \psi_0^{\shortmid\,\mathrm{PD}}\,\mathrm{d}V^{\shortmid}$ | $\Psi_0 = \left[\frac{\rho_0}{\rho_0^*}\right]^n \Psi_0^{\mathrm{CCM}}$ |
| mass source | $\mathcal{R}_0 = c\left[\left[\frac{\rho_0}{\rho_0^*}\right]^{-m}\Psi_0 - \Psi_0^*\right]$ | $\mathcal{R}_0 = c\left[\left[\frac{\rho_0}{\rho_0^*}\right]^{-m}\Psi_0 - \Psi_0^*\right]$ |

derivative of a quantity $\{\bullet\}$ at fixed material placement $\boldsymbol{X}$ is denoted by $\mathrm{D}_t\{\bullet\}$. Densities per unit volume are denoted by $\{\bullet\}_0$. The material density $\rho_0$ of the continuum point and $\rho_0^{\shortmid}$ of its neighbours are local continuum quantities. They are considered homogenised versions of the underlying open-pored bone tissue.

### 2.2. Governing equations

In the following, we only state the balance equations for our PD formulation. For the sake of completeness the corresponding balance equations for CCM can be found in Table 1.

#### 2.2.1. Balance of mass

In our peridynamic formulation, the point-wise balance of mass is given by

$$\mathrm{D}_t\rho_0 = \mathcal{R}_0, \tag{4}$$

where $\rho_0$ is the point density and $\mathcal{R}_0$ the scalar mass source term. Note that similar to CCM we consider the balance of mass as a local balance equation. However, $\mathcal{R}_0$ can be a nonlocal quantity by its constitutive equation. For the sake of simplicity, we do not consider a mass flux term as proposed in Kuhl and Steinmann (2003) and discussed in Papastavrou, Schmidt, Deng et al. (2020).

#### 2.2.2. Balance of linear and angular momentum

The point-wise balance of linear momentum equilibrates the temporal rate of the momentum density $\boldsymbol{\pi}_0 = \rho_0\boldsymbol{v}$ with the internal body force density $\boldsymbol{b}_0^{\mathrm{int}}$ and the external body force density $\boldsymbol{b}_0^{\mathrm{ext}}$ as

$$\mathrm{D}_t\boldsymbol{\pi}_0 = \boldsymbol{b}_0^{\mathrm{int}} + \boldsymbol{b}_0^{\mathrm{ext}} \quad \text{with} \quad \boldsymbol{b}_0^{\mathrm{ext}} := \bar{\boldsymbol{b}}_0^{\mathrm{ext}} + \boldsymbol{v}\mathcal{R}_0, \tag{5}$$

where $\bar{\boldsymbol{b}}_0^{\mathrm{ext}}$ is the external body force density reduced by the additional source term $\boldsymbol{v}\mathcal{R}_0$ due the mass source $\mathcal{R}_0$. The internal body force $\boldsymbol{b}_0^{\mathrm{int}}$ is given by an integral of the pairwise force density $\boldsymbol{p}^{\shortmid}$ between the continuum point $\boldsymbol{X}$ and its neighbours $\boldsymbol{X}^{\shortmid}$ over the horizon $\mathcal{H}_0$ as

$$\boldsymbol{b}_0^{\mathrm{int}} = \int_{\mathcal{H}_0} \boldsymbol{p}^{\shortmid}\,\mathrm{d}V^{\shortmid}, \tag{6}$$

see Javili et al. (2019).

The reduced format of the balance of linear momentum (5) is obtained by incorporating the balance of mass (4) into Eq. (5), resulting in

$$\rho_0\mathrm{D}_t\boldsymbol{v} = \int_{\mathcal{H}_0} \boldsymbol{p}^{\shortmid}\,\mathrm{d}V^{\shortmid} + \bar{\boldsymbol{b}}_0^{\mathrm{ext}}. \tag{7}$$

In the following, we neglect the inertia term $\rho_0\mathrm{D}_t\boldsymbol{v}$ as the time scales of the remodelling process and the inertia are significantly different, see Frost (1987). Body forces, induced by gravity, are neglected as well, since the loads induced by locomotion are far greater and the governing factor for the remodelling process, see Jacobs et al. (1995). Accordingly, the balance of linear momentum (7) is reduced to the equilibrium condition for the internal body force density

$$\int_{\mathcal{H}_0} \boldsymbol{p}^{\shortmid}\,\mathrm{d}V^{\shortmid} = \boldsymbol{0}. \tag{8}$$

The balance of angular momentum is obtained following the derivation outlined in Javili et al. (2019), and reads eventually

$$\int_{\mathcal{H}_0} \boldsymbol{\xi}^{\shortmid} \times \boldsymbol{p}^{\shortmid}\,\mathrm{d}V^{\shortmid} = \boldsymbol{0}. \tag{9}$$

It is shown in Javili et al. (2019) that the balance of angular momentum is satisfied a priori for one-neighbour interactions when the pairwise force density $\boldsymbol{p}^{\shortmid} = \zeta\boldsymbol{\xi}^{\shortmid}$ is coaxial to $\boldsymbol{\xi}^{\shortmid}$ with a scaling $\zeta = \zeta(\boldsymbol{\xi}^{\shortmid})$, which itself is an arbitrary (scalar) function of $\boldsymbol{\xi}^{\shortmid}$. Since we fulfil this requirement in the following, the balance of angular moment is satisfied a priori and is here only stated for the sake of completeness.

### 2.3. Constitutive expressions

The constitutive equations for our peridynamic model are obtained assuming isothermal conditions. In general,

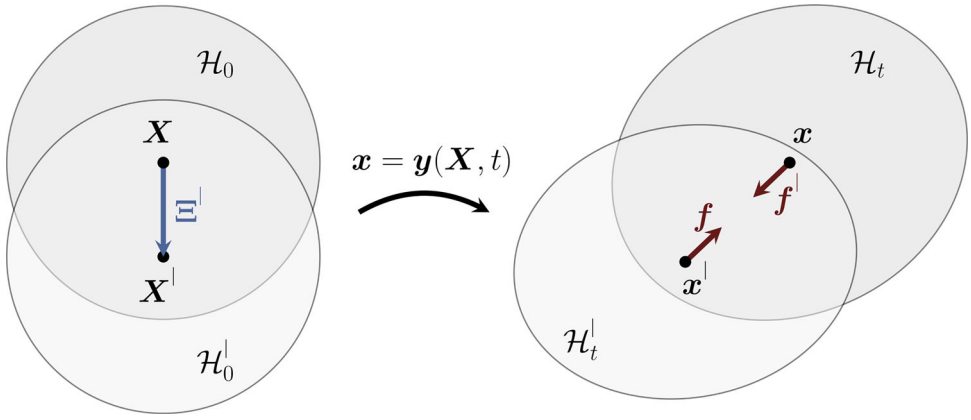


**Figure 2.** Resulting interaction forces between point $\boldsymbol{x}$ and neighbour $\boldsymbol{x}^{|}$ in the spatial configuration (right) due to a deformation of the material configuration (left). The interaction forces with the same magnitude are equivalent to bond-based PD in the framework of Silling (2000).

the volume-specific energy density function at a continuum point in PD is given in integral form over $\mathcal{H}_0$ as

$$\Psi_0 = \frac{1}{2}\int_{\mathcal{H}_0} \psi_0^{|}\, \mathrm{d}V^{|}, \tag{10}$$

where $\psi_0^{|}$ is the volume-specific pairwise energy density function with units $\mathrm{Nm/m^6}$. The weighting factor of one half is introduced to avoid double counting of energy between two continuum points, since we are visiting every continuum point twice when considering the global form of the balance equations.

Modelling bone as open-pored hard tissue, the energy density $\Psi_0$ in CCM is weighted with a power of the nominal relative density, see Carter and Hayes (1977) and Harrigan and Hamilton (1993). To apply this approach to the nonlocal formulation in a peridynamic sense, we weight the pairwise energy density $\psi_0^{|}$ with a power of the nominal relative density, resulting in

$$\Psi_0 = \frac{1}{2}\int_{\mathcal{H}_0} \left[\frac{\hat{\rho}_0^{|}}{\rho_0^*}\right]^n \psi_0^{|\,\mathrm{PD}} \mathrm{d}V^{|} \quad \text{with} \quad \hat{\rho}_0^{|} = \frac{1}{2}\left[\rho_0 + \rho_0^{|}\right], \tag{11}$$

where $\psi_0^{|\,\mathrm{PD}}$ denotes the density-independent pairwise energy density function that governs the purely mechanical material behaviour. The volume-specific energy density $\psi_0^{|}$ from Eq. (10) is thus related to $\psi_0^{|\,\mathrm{PD}}$ via

$$\psi_0^{|} = \left[\frac{\hat{\rho}_0^{|}}{\rho_0^*}\right]^n \psi_0^{|\,\mathrm{PD}}. \tag{12}$$

Note that we additionally introduce the nominal relative density in a nonlocal sense, as it is dependent on the arithmetic mean density $\hat{\rho}_0^{|}$ of the density $\rho_0$ at the continuum point and $\rho_0^{|}$ of its neighbours, and the initial density $\rho_0^*$ at time $t_0$. By doing so, we maintain the definition of bond-based PD, where two continuum points exert forces with same magnitude on each other, as depicted in Figure 2. The exponent $n$ in Eq. (11) represents a material parameter for the porosity of bone tissue. In CCM, it is determined empirically, see Gibson (2005), and varies between $1 \leq n \leq 3.5$. The mechanical material behaviour for open-pored hard tissue is typically modelled with an elastic energy density, see Gibson and Ashby (1982), which motivates why we maintain the volume-specific harmonic pairwise energy density function

$$\psi_0^{|\,\mathrm{PD}} = \frac{1}{2} CL\left[\frac{l}{L} - 1\right]^2, \tag{13}$$

between two continuum points, as it is widely used in PD literature, see Silling and Askari (2005) or Javili et al. (2019). The peridynamic material parameter $C$ for bond-based PD is an indicator for the resistance against the change of bond length. Also, $L = |\boldsymbol{\Xi}^{|}|$ and $l = |\boldsymbol{\xi}^{|}|$ denote the bond lengths in the material and spatial configurations, respectively.

The constitutive equation for the pairwise force density $\boldsymbol{p}^{|}$ acting on a continuum point due to mechanical interactions with a continuum point in its finite neighbourhood is given by

$$\boldsymbol{p}^{|} := \frac{\partial \psi_0^{|}}{\partial \boldsymbol{\xi}^{|}}. \tag{14}$$

Inserting Eq. (12) into (14), we obtain

$$\boldsymbol{p}^{|} = \left[\frac{\hat{\rho}_0^{|}}{\rho_0^*}\right]^n \boldsymbol{p}^{|\,\mathrm{PD}} \qquad \text{with} \qquad \boldsymbol{p}^{|\,\mathrm{PD}} := \frac{\partial \psi_0^{|\,\mathrm{PD}}}{\partial \boldsymbol{\xi}^{|}}. \tag{15}$$

As bone tissue tends to reach a biological equilibrium state (homeostasis), the mass source function typically considers the difference between the weighted volume-specific energy density $\Psi_0$ and the attractor

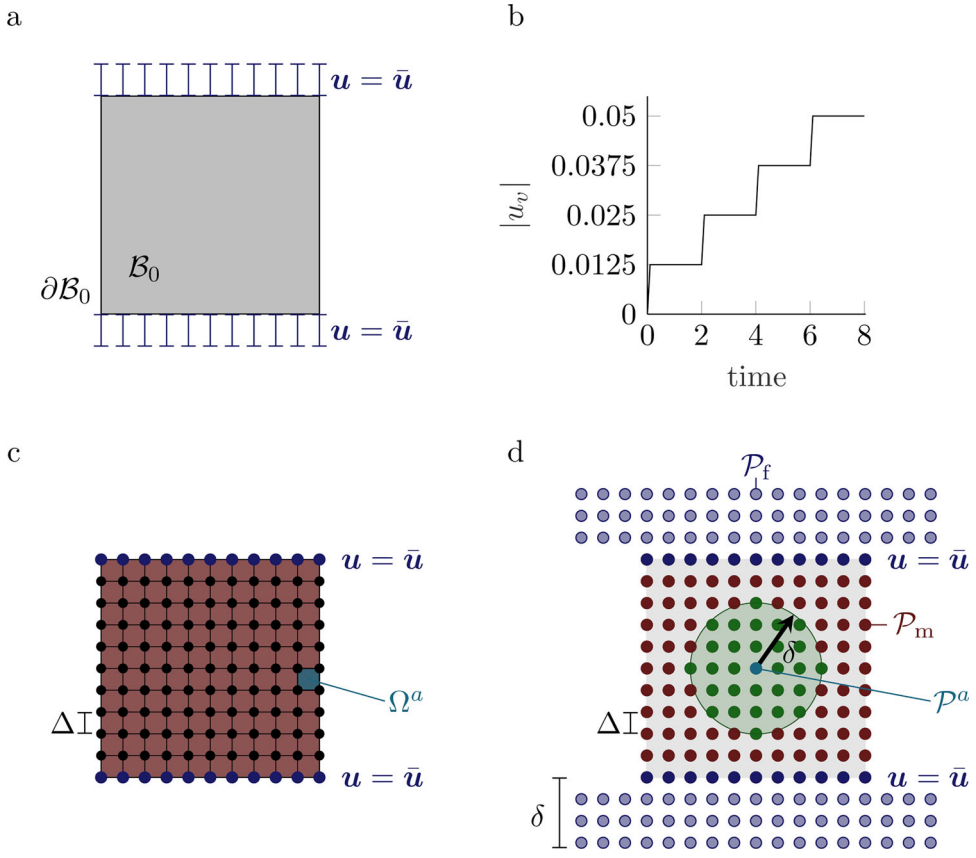


**Figure 3.** Schematic illustration of a unit square with prescribed displacement $\boldsymbol{u} = [u_h \; u_v]$ at the upper and lower edge in its continuum form (a). The magnitude of the prescribed displacement in vertical direction $|u_v|$ is a stepwise displacement function (b). The spatial discretisation in FEM implies the discretisation of a continuum body $\mathcal{B}_0$ in a finite number of elements $\Omega^a$ (c) and in PD in a finite number of *collocation points* $\mathcal{P}^a$ (d). In terms of the PD discretisation (d), $\mathcal{P}_\mathrm{m}$ denotes the material and $\mathcal{P}_\mathrm{f}$ the fictitious *collocation points*.

stimulus $\Psi_0^*$, see (Harrigan and Hamilton 1993; Kuhl and Steinmann 2003; Papastavrou, Schmidt, Deng et al. 2020; Papastavrou, Schmidt and Steinmann 2020; Schmidt et al. 2021). In the following, the mass source term is given by

$$\mathcal{R}_0 = c\left[\left[\frac{\rho_0}{\rho_0^*}\right]^{-m}\Psi_0 - \Psi_0^*\right], \tag{16}$$

where the parameter $c$ governs the rate of the biomechanical process. The stability of the mass source function is thereby determined by the dimensionless exponent $m$. The relation $n < m$ ensures numerical stability, see Harrigan and Hamilton (1993) and uniqueness of solutions, see Harrigan and Hamilton (1994). Note that $\mathcal{R}_0$ in our PD formulation differs from the CCM formulation only by the nonlocality of the volume-specific energy density $\Psi_0$ in Eq. (11), see Table 1.

## 3. Computational implementation

The presented biomechanical PD model needs to satisfy both balances of mass (4) and linear momentum (8) at every space-time point, in addition to the angular momentum balance (9) that is a priori fulfilled. Due to the time dependent and nonlinear coupled equations, we use an implicit Euler scheme with an incremental step of $\Delta t_{\mathrm{n}+1} = t_{\mathrm{n}+1} - t_\mathrm{n}$ for the temporal discretisation. The biological and mechanical residual of our boundary value problem in a temporal discretised form are given by

$$\begin{aligned}{}^{\rho}R_{\mathrm{n}+1} = &-\rho_{0_{\mathrm{n}+1}} + \rho_{0_\mathrm{n}} \\ &+ c\left[\left[\frac{\rho_{0_{\mathrm{n}+1}}}{\rho_0^*}\right]^{-m}\frac{1}{2}\int_{\mathcal{H}_0}\left[\frac{\hat{\rho}^{|}_{0_{\mathrm{n}+1}}}{\rho_0^*}\right]^{n}\psi^{|\mathrm{PD}}_{0_{n+1}}\,\mathrm{d}V^{|}\right. \\ &\left.-\Psi_0^*\right]\Delta t_{\mathrm{n}+1} \doteq 0,\end{aligned} \tag{17}$$

and

$${}^{\boldsymbol{x}}\boldsymbol{R}_{\mathrm{n}+1} = \int_{\mathcal{H}_0}\left[\frac{\hat{\rho}^{|}_{0_{\mathrm{n}+1}}}{\rho_0^*}\right]^{n}\boldsymbol{p}^{|\mathrm{PD}}_{\mathrm{n}+1}\mathrm{d}V^{|} \doteq \boldsymbol{0}, \tag{18}$$

for the time step $t_{\mathrm{n}+1}$, indicated by the subscript $n+1$.

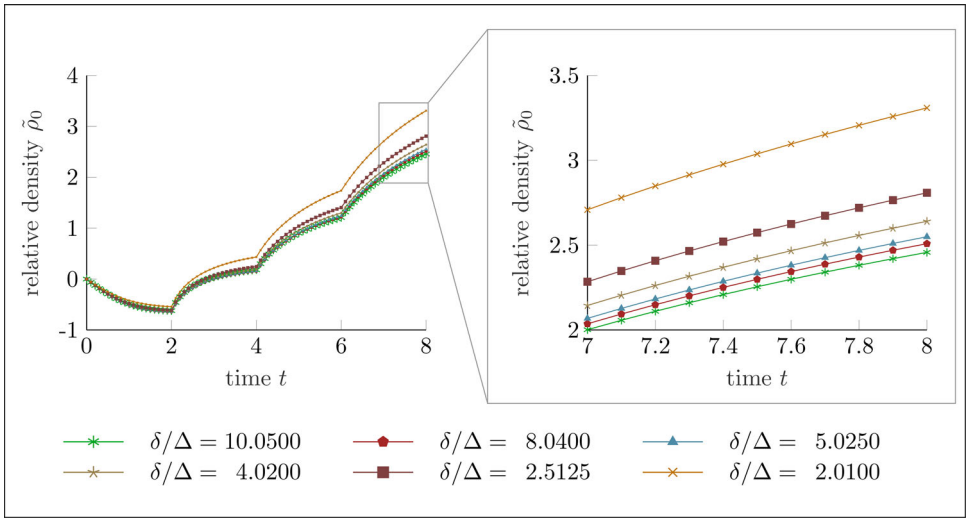


**Figure 4.** Evolution of the mean value over all material points of the relative density $\tilde{\rho}_0 = [\rho_0 - \rho_0^*]/\rho_0^*$ for a fixed horizon size $\delta = 0.05025$ and varying ratios $\delta/\Delta = \{2.01,\ 2.5125,\ 4.02,\ 5.025,\ 8.04,\ 10.05\}$, resulting from a symmetrically applied stepwise displacement function, schematically depicted in Figure 3.

Furthermore, we spatially discretise the domain into a finite number of *collocation points* at which we evaluate the discretised balance equations (17) and (18). Hence, the integrals over the horizon $\mathcal{H}_0$ need to be replaced by a summation over *quadrature points* representing the neighbourhood. In this contribution, we use the *collocation points* as *quadrature points* in $\mathcal{H}_0$. Thus, the temporal and spatial discretised residuals for the *collocation point* $\mathcal{P}^a$ read

$$
\begin{aligned}
{}^{\rho}\mathbb{R}^a_{\mathrm{n}+1} = &-\rho^a_{0_{\mathrm{n}+1}} + \rho^a_{0_{\mathrm{n}}} \\
&+ c\left[\left[\frac{\rho^a_{0_{\mathrm{n}+1}}}{\rho^*_0}\right]^{-m} \frac{1}{2}\sum_{\substack{i=1\\ i\neq a}}^{\mathcal{N}} \left[\frac{\hat{\rho}^{|}_{0_{i_{\mathrm{n}+1}}}}{\rho^*_0}\right]^{n} \hat{\rho}^{|\ \mathrm{PD}}_{0_{i_{\mathrm{n}+1}}} V^{|}_i \right. \\
&\left. - \boldsymbol{\Psi}^*_0\right] \Delta t_{\mathrm{n}+1} \doteq 0,
\end{aligned}
\tag{19}
$$

and

$$
{}^{\boldsymbol{x}}\mathbb{R}^a_{\mathrm{n}+1} = \sum_{\substack{i=1\\ i\neq a}}^{\mathcal{N}} \left[\frac{\hat{\rho}^{|}_{0_{i_{\mathrm{n}+1}}}}{\rho^*_0}\right]^{n} C\left[\frac{1}{|\boldsymbol{\Xi}^{|}_{i_{\mathrm{n}+1}}|} - \frac{1}{|\boldsymbol{\xi}^{|}_{i_{\mathrm{n}+1}}|}\right] \boldsymbol{\xi}^{|}_{i_{\mathrm{n}+1}} V^{|}_i \doteq \mathbf{0},
\tag{20}
$$

where $\mathcal{N}$ is the number of (collocation) points in the horizon $\mathcal{H}_0$. The quantities within the summation are quantities related to point $\mathcal{P}^a$ and neighbour $\mathcal{P}^i$. The volume $V^{|}_i$ assigned to each neighbour serves as weighting factor for the numerical integration.

To solve the coupled nonlinear problem numerically, we use an iterative Newton–Raphson scheme. The linearisation of the residuals (19) and (20) leads to

$$
{}^{\rho}\mathbb{R}^a_{k+1} = {}^{\rho}\mathbb{R}^a_k + \underbrace{\left.\frac{\partial {}^{\rho}\mathbb{R}^a}{\partial \rho^b}\right|_k}_{{}^{\rho\rho}\mathbb{K}^{ab}_k} \Delta\rho^b_k + \underbrace{\left.\frac{\partial {}^{\rho}\mathbb{R}^a}{\partial \mathbb{x}^b}\right|_k}_{{}^{\rho\boldsymbol{x}}\mathbb{K}^{ab}_k} \cdot \Delta\mathbb{x}^b_k \doteq 0,
\tag{21}
$$

and

$$
{}^{\boldsymbol{x}}\mathbb{R}^a_{k+1} = {}^{\boldsymbol{x}}\mathbb{R}^a_k + \underbrace{\left.\frac{\partial {}^{\boldsymbol{x}}\mathbb{R}^a}{\partial \rho^b}\right|_k}_{{}^{\boldsymbol{x}\rho}\mathbb{K}^{ab}_k} \Delta\rho^b_k + \underbrace{\left.\frac{\partial {}^{\boldsymbol{x}}\mathbb{R}^a}{\partial \mathbb{x}^b}\right|_k}_{{}^{\boldsymbol{x}\boldsymbol{x}}\mathbb{K}^{ab}_k} \cdot \Delta\mathbb{x}^b_k \doteq \mathbf{0},
\tag{22}
$$

for the $k$th iteration. Next, we establish the global residual (column) vector $\mathbb{R} = \left[{}^{\rho}\mathbb{R}\ {}^{\boldsymbol{x}}\mathbb{R}\right]^T$, where ${}^{\rho}\mathbb{R}$ and ${}^{\boldsymbol{x}}\mathbb{R}$ are assembled by the point-wise residuals following ${}^{*}\mathbb{R} = \left[{}^{*}\mathbb{R}^1\ {}^{*}\mathbb{R}^2\ \cdots\ {}^{*}\mathbb{R}^a\ \cdots\ {}^{*}\mathbb{R}^{\mathcal{P}}\right]^T$ with $* = \{\rho,\ \boldsymbol{x}\}$. The asterisk is introduced for the sake of brevity and stands for the field variables $\rho$ and $\boldsymbol{x}$, respectively.

The global tangent of the system $\mathbb{K}$ is composed as

$$
\mathbb{K} = \begin{bmatrix} {}^{\rho\rho}\mathbb{K} & {}^{\rho\boldsymbol{x}}\mathbb{K} \\ {}^{\boldsymbol{x}\rho}\mathbb{K} & {}^{\boldsymbol{x}\boldsymbol{x}}\mathbb{K} \end{bmatrix},
$$

where the stiffness sub-matrices ${}^{\rho\rho}\mathbb{K}$, ${}^{\rho\boldsymbol{x}}\mathbb{K}$, ${}^{\boldsymbol{x}\rho}\mathbb{K}$ and ${}^{\boldsymbol{x}\boldsymbol{x}}\mathbb{K}$ are assembled as following

$$
{}^{**}\mathbb{K} = \begin{bmatrix}
{}^{**}\mathbb{K}^{11} & {}^{**}\mathbb{K}^{12} & \cdots & {}^{**}\mathbb{K}^{1b} & \cdots & {}^{**}\mathbb{K}^{1\mathcal{P}} \\
{}^{**}\mathbb{K}^{21} & {}^{**}\mathbb{K}^{22} & \cdots & {}^{**}\mathbb{K}^{2b} & \cdots & {}^{**}\mathbb{K}^{2\mathcal{P}} \\
\vdots & \vdots & \vdots & \vdots & \vdots & \vdots \\
{}^{**}\mathbb{K}^{a1} & {}^{**}\mathbb{K}^{a2} & \cdots & {}^{**}\mathbb{K}^{ab} & \cdots & {}^{**}\mathbb{K}^{a\mathcal{P}} \\
\vdots & \vdots & \vdots & \vdots & \vdots & \vdots \\
{}^{**}\mathbb{K}^{\mathcal{P}1} & {}^{**}\mathbb{K}^{\mathcal{P}2} & \cdots & {}^{**}\mathbb{K}^{\mathcal{P}b} & \cdots & {}^{**}\mathbb{K}^{\mathcal{P}\mathcal{P}}
\end{bmatrix}
$$

with $** = \{\rho\rho,\ \rho\boldsymbol{x},\ \boldsymbol{x}\rho,\ \boldsymbol{x}\boldsymbol{x}\}$.

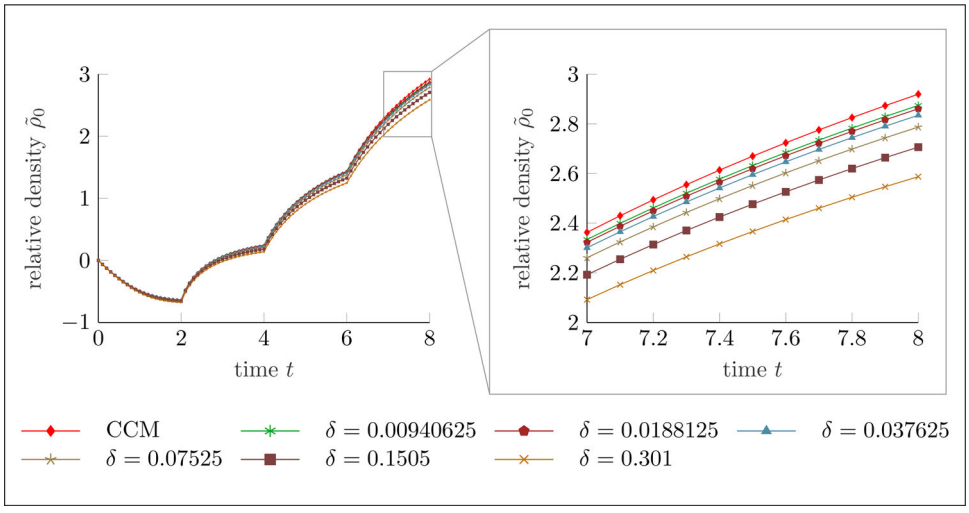


**Figure 5.** Evolution of the mean value over all material points of the relative density $\tilde{\rho}_0 = [\rho_0 - \rho_0^*]/\rho_0^*$ for a fixed ratio $\delta/\Delta = 3.01$ and varying horizon size $\delta = \{0.00940625,\ 0.0188125,\ 0.037625,\ 0.07525,\ 0.1505,\ 0.301\}$, resulting from a symmetrically applied stepwise displacement function, schematically depicted in Figure 3.

The resulting incremental update for the discretised density $\rho_{k+1} = \rho_k + \Delta\rho_k$ and the discretised placement $\mathbb{x}_{k+1} = \mathbb{x}_k + \Delta\mathbb{x}_k$ are obtained by using $[\Delta\rho\ \ \Delta\mathbb{x}]^T = -\mathbb{K}^{-1} \cdot \mathbb{R}$ at the $k$th iteration to solve the system of equations from Eqs. (21) and (22) for the unknown quantities $\Delta\rho_k$ and $\Delta\mathbb{x}_k$. The iteration scheme is repeated until the norm of $\mathbb{R}$ falls below a sufficiently small prescribed tolerance.

The detailed computation of the stiffness submatrices ${}^{\rho\rho}\mathbb{K}^{ab}$, ${}^{\rho\boldsymbol{x}}\mathbb{K}^{ab}$, ${}^{\boldsymbol{x}\rho}\mathbb{K}^{ab}$ and ${}^{\boldsymbol{xx}}\mathbb{K}^{ab}$ are given in Appendix A. For more details on the computational implementation we refer to Javili et al. (2020).

## 4. Numerical examples

We demonstrate the characteristics of our peridynamic bone remodelling formulation with two two-dimensional numerical examples. First, we validate the nonlocal formulation for the sake of demonstration with a simple geometry of a unit square under symmetric displacement loading. Therein, we first perform a convergence study concerning the integration over the horizon, where we fix the horizon size $\delta$ and vary the ratio $\delta/\Delta$ with $\Delta$ being the grid spacing in vertical and horizontal directions. For a second convergence study concerning the influence of nonlocality, we fix the ratio $\delta/\Delta$ and vary $\delta$.

As a second numerical example, we illustrate the resulting density distribution throughout the proximal femur which occurs due to daily locomotion. To highlight the influence of nonlocality in our peridynamic model for this realistic example, we vary the horizon size $\delta$.

For both examples we compare the PD results with a respective CCM solution, obtained using the finite element method (FEM). Therein, we utilise a St. Venant–Kirchhoff material model that is appropriate to compare with the harmonic energy density in Eq. (13). Thus, the volume-specific energy density of a compressible Neo–Hooke-type material $\Psi_0^{\text{CCM}} = \Psi_0^{\text{Neo}}$, commonly used for bone remodelling in Buganza Tepole and Kuhl (2016), Kuhl and Steinmann (2003), Papastavrou, Schmidt, Deng et al. (2020), Papastavrou, Schmidt and Steinmann (2020) and Schmidt et al. (2021), is replaced by the St. Venant–Kirchhoff energy density

$$\Psi_0^{\text{CCM}} = \Psi_0^{\text{StVK}} = \frac{1}{2}\lambda[\text{Tr}(\mathbf{E})]^2 + \mu\text{Tr}(\mathbf{E}^2) \quad \text{with} \quad \mathbf{E} = \frac{1}{2}[\mathbf{F}^{\text{T}}\mathbf{F} - \mathbf{1}], \tag{23}$$

and the classical Lamé constants $\lambda$ and $\mu$. The Green–Lagrange strain tensor $\mathbf{E}$ is a function of the deformation gradient $\mathbf{F} := \text{Grad}\ \boldsymbol{y}$. With respect to the equations given in Table 1, we thus equate the energy density $\Psi_0^{\text{CCM}}$ with $\Psi_0^{\text{StVK}}$ for the CCM model. We expect that the PD results converge towards the local solution when a small horizon size is used compared to the domain size. It is worth mentioning that a comparison of a FEM simulation with a Neo–Hookean and a St. Venant–Kirchhoff material model does not result in significant differences in the density evolution. For all FEM simulations we use the formulation presented in Papastavrou, Schmidt, Deng et al. (2020) and Papastavrou, Schmidt and Steinmann (2020) with a bi-linear element expansions and a $2 \times 2$ Gauss quadrature rule.

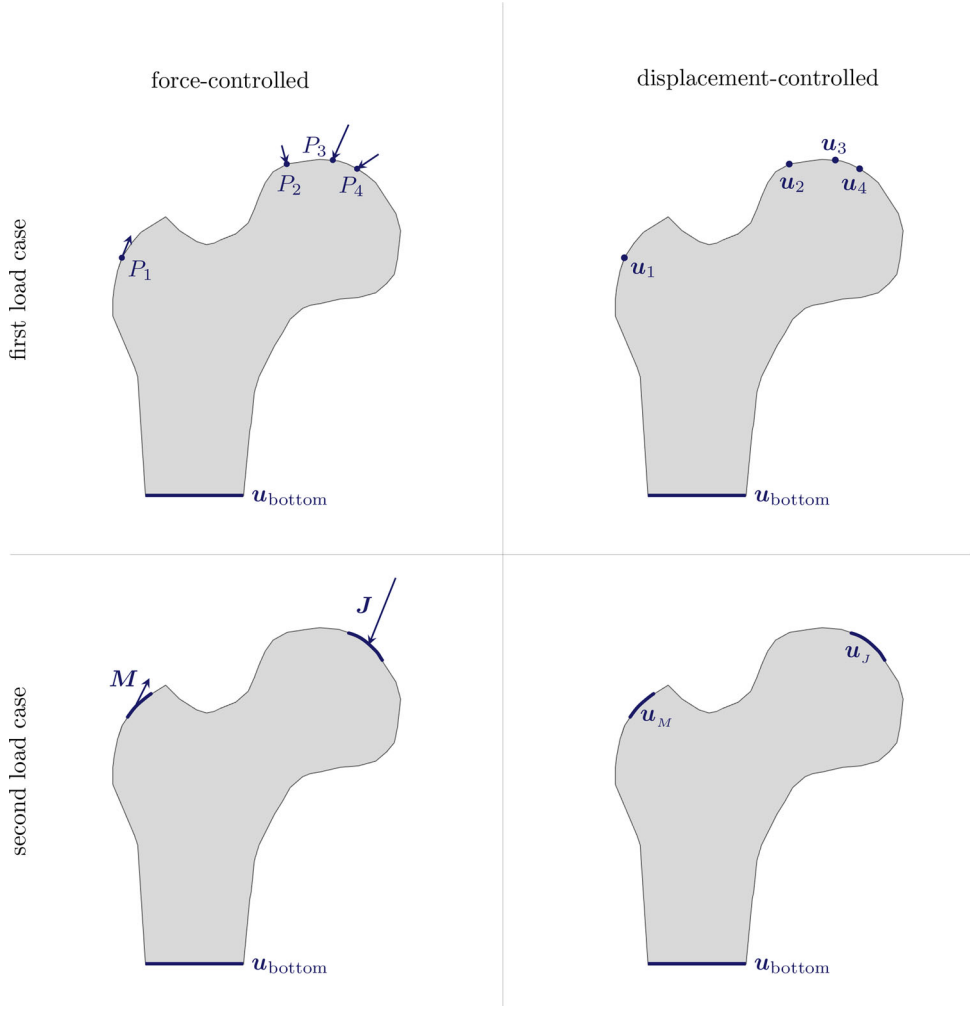


**Figure 6.** Schematic illustration of two load cases applied on the proximal femur. First load case with point-wise Neumann boundary conditions (top left) at four points $P_1$, $P_2$, $P_3$ and $P_4$. Second load case with forces $M$ and $J$ that are applied as distributed forces for the force-controlled simulation (bottom left). The resulting displacements $u_1$, $u_2$, $u_3$ and $u_4$ of the first load case and $u_M$ and $u_J$ of the second load case are prescribed as Dirichlet boundary conditions for the displacement-controlled simulations (right).

### 4.1. Unit square

We prescribe a displacement $\bar{u} = \bar{u}(t)$ on the upper and lower edge of a unit square in vertical direction, which is increased stepwise over time, as schematically depicted in Figure 3. For prescribing Dirichlet boundary conditions in PD, we add a fictitious material layer with thickness $\delta$, as depicted in Figure 3d. The displacement at the fictitious points $\mathcal{P}_f$ are set such that the required bond stretch is reflected in the material layer. The initial density of the unit square is uniformly set to $\rho_0^* = 1.0$ and the Young's modulus to $E = 1.0$. The peridynamic material parameter $C$ is computed according to $E$ by comparing the energy densities in Eqs. (13) and (23) for a biaxial deformation.

Note that $E$ and $C$ are initial homogenised parameters, since the presented model is homogenised at the macroscale. Although the homogenised stiffness parameters, $E$ and $C$, enter the energy density functions $\Psi_0^{CCM}$ and $\psi_0^{\text{PD}}$, respectively, as constant parameters, the stiffness of the material varies in time due to the weighting with the time-dependent relative nominal density, see Table 1. A detailed discussion on the conversion between the *true* material parameters at the microscale and homogenised (*nominal*) ones at the macroscale is addressed in Schmidt et al. (2021).

With only one-neighbour interactions (or bond-based PD) the Poisson ratio is fixed to 1/3 as demonstrated in Javili et al. (2020), and it is set accordingly for the FEM simulation. We simulate four loading steps with a load-step time of $T = 2$ and an incremental time step of $\Delta t = 0.1$. As we prescribe a displacement function $\bar{u}(t)$ instead of a force function, as considered in Kuhl et al. (2003), Kuhl and Steinmann (2003), Papastavrou, Schmidt, Deng et al. (2020), Papastavrou, Schmidt and Steinmann (2020) and Schmidt et al. (2021), we adjust the material parameters for the mass

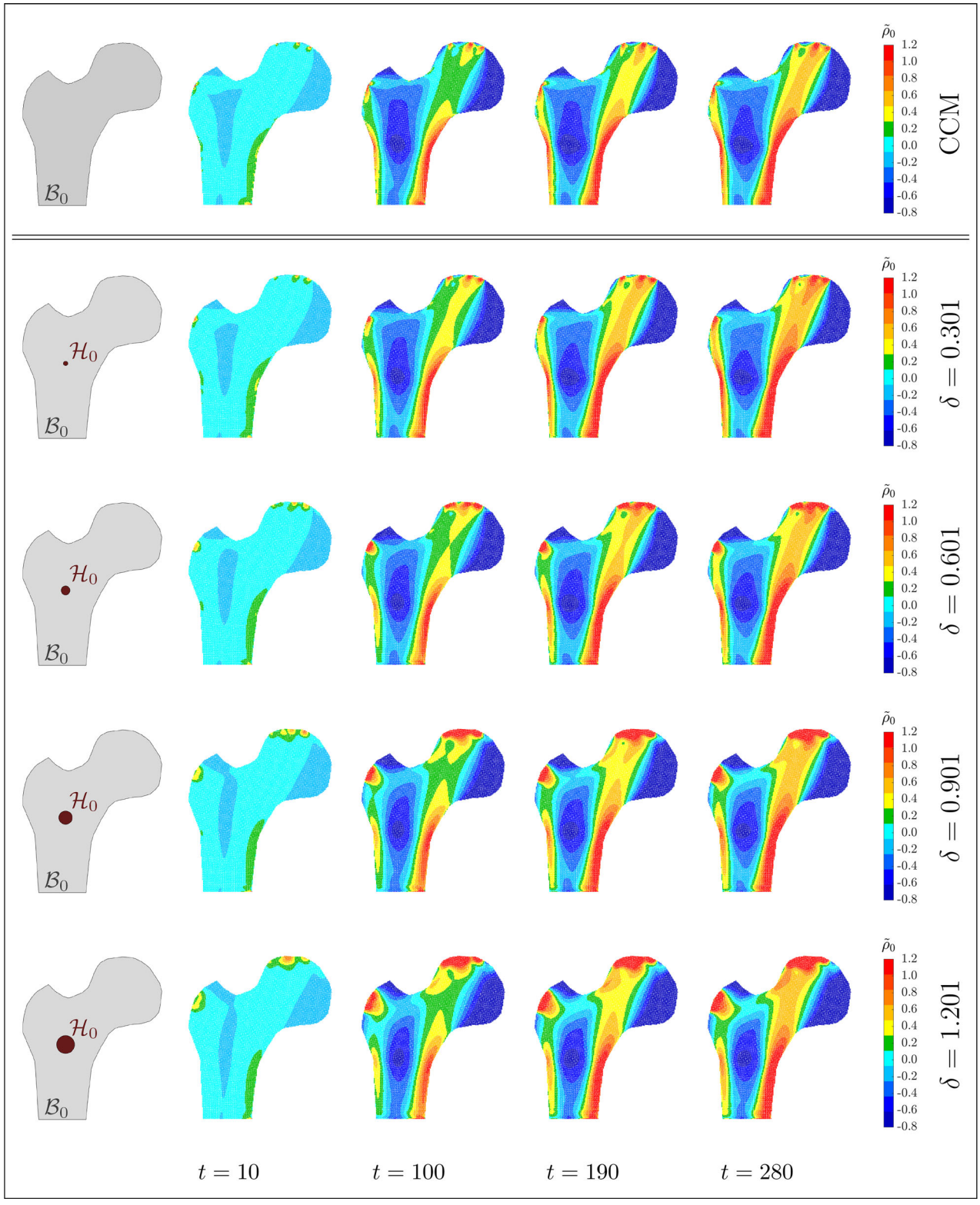


**Figure 7.** Distribution of the relative density $\tilde{\rho}_0 = [\rho_0 - \rho_0^*]/\rho_0^*$ for the simulations of the first load case. The resulting relative density distribution throughout the proximal femur is given for different time points $t = \{10,\ 100,\ 190,\ 280\}$ and horizon sizes $\delta = \{0.301,\ 0.601,\ 0.901,\ 1.201\}$ at fixed $\Delta = 0.1$. In the top row, the CCM results are depicted for comparison.

source term to obtain an appropriate density evolution. The density growth velocity parameter is set to $c = 1000$, the attractor stimulus to $\Psi_0^* = 0.01$ and the exponents to $n = 2$ and $m = 3$, respectively.

In the following section, we discuss two convergence studies. First, we fix the horizon size to $\delta = 0.05025$ and vary the grid spacing $\Delta = \{0.025,\ 0.02,\ 0.0125,\ 0.01, 0.00625,\ 0.005\}$ resulting in ratios

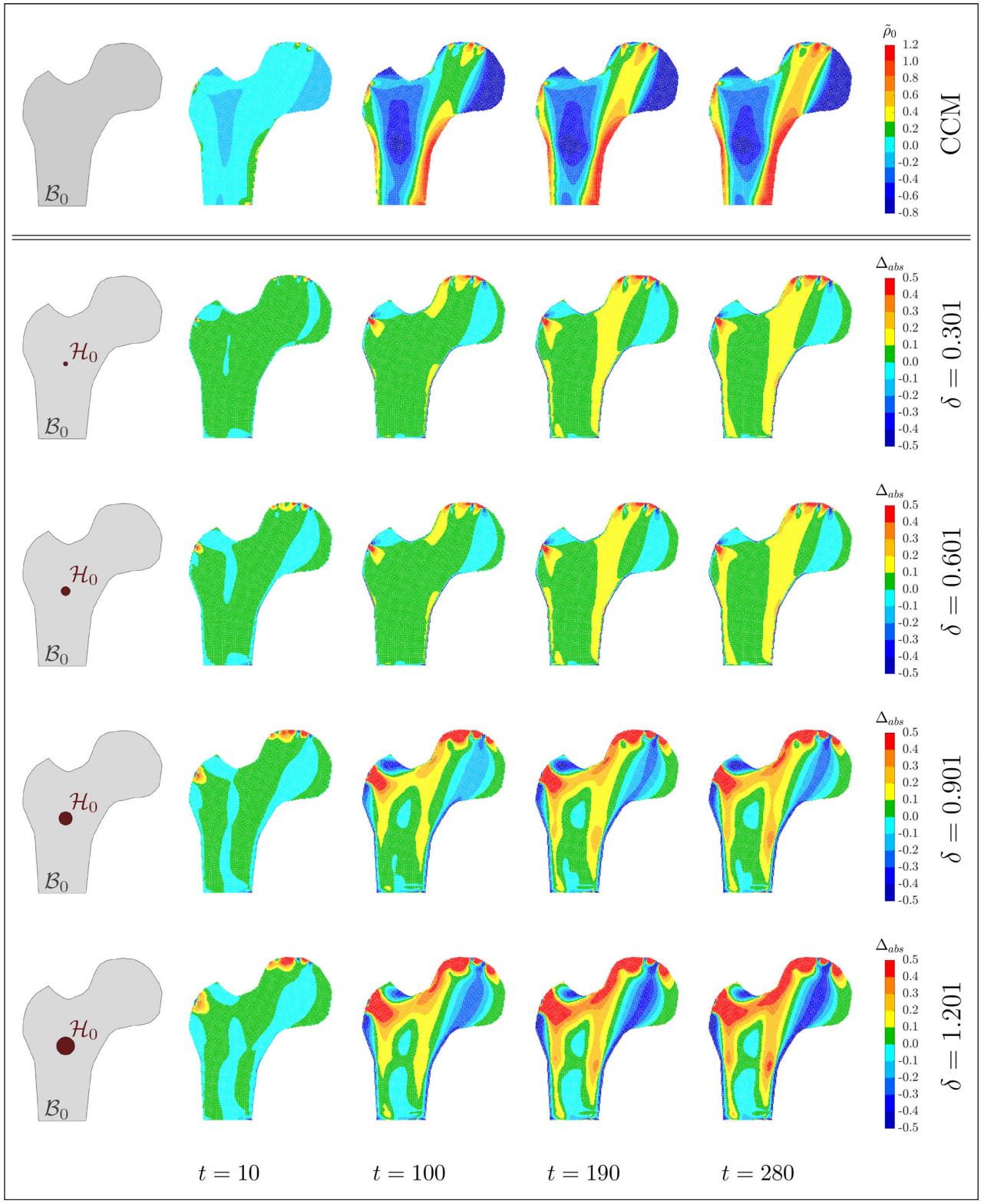


**Figure 8.** Distribution of the absolute change $\Delta_{abs} = \tilde{\rho}_{0_{PD}} - \tilde{\rho}_{0_{FEM}}$ for the simulations of the first load case. The resulting absolute change throughout the proximal femur is given for different time points $t = \{10,\ 100,\ 190,\ 280\}$ and horizon sizes $\delta = \{0.301,\ 0.601,\ 0.901,\ 1.201\}$ at fixed $\Delta = 0.1$. In the top row, the CCM results are depicted for comparison.

$\delta/\Delta = \{2.01,\ 2.5125,\ 4.02,\ 5.025,\ 8.04,\ 10.05\}$. We expect that with increasing ratio $\delta/\Delta$ the solution converges to a more accurate solution as the number of neighbours and thus integration points in the horizon increases. The resulting mean value over all material points of the relative density $\tilde{\rho}_0 =$

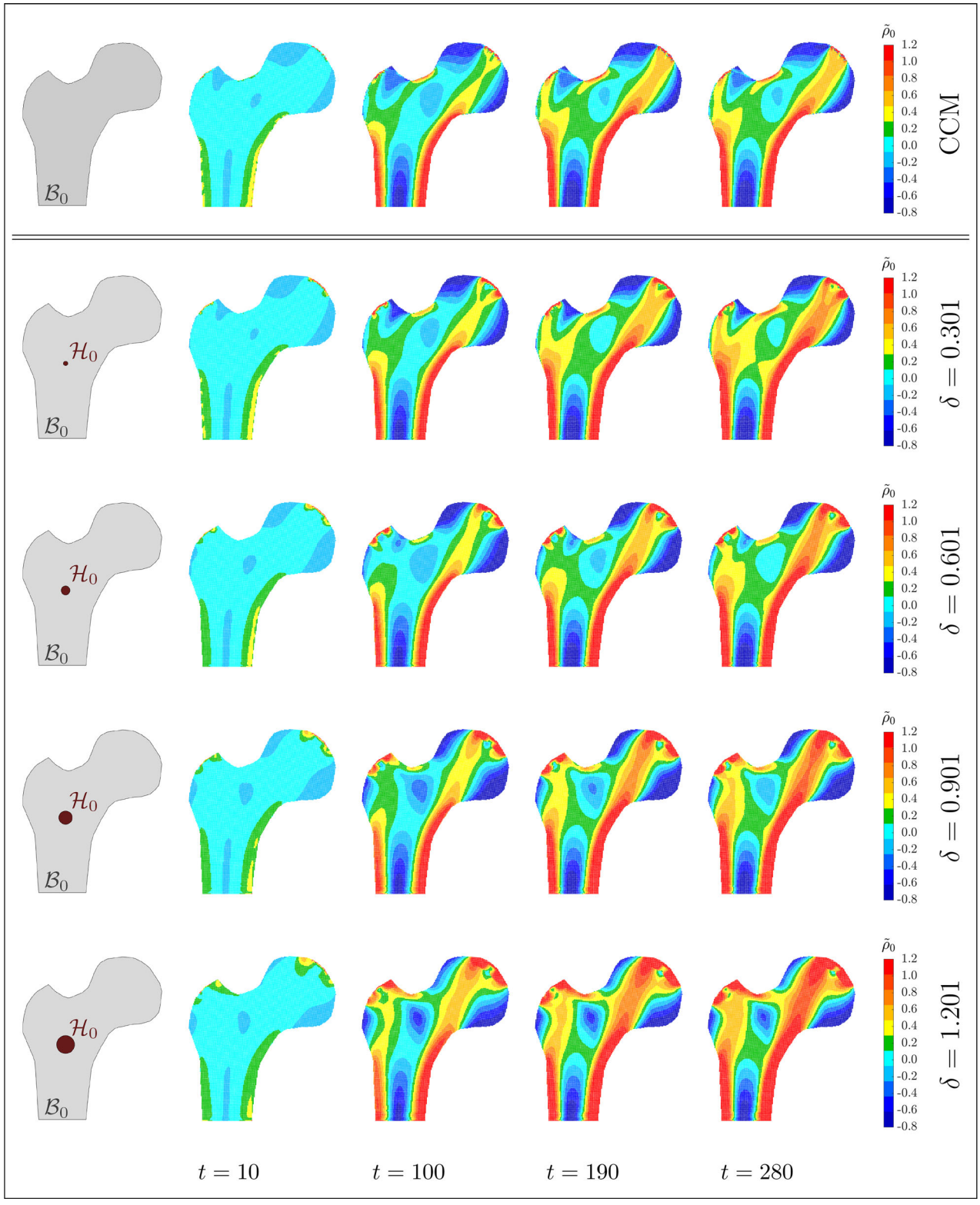


**Figure 9.** Distribution of the relative density $\tilde{\rho}_0 = [\rho_0 - \rho_0^*]/\rho_0^*$ for the simulations of the second load case. The resulting relative density distribution throughout the proximal femur is given for different time points $t = \{10,\ 100,\ 190,\ 280\}$ and horizon sizes $\delta = \{0.301,\ 0.601,\ 0.901,\ 1.201\}$ at fixed $\Delta = 0.1$. In the top row, the CCM results are given for comparison.

$[\rho_0 - \rho_0^*]/\rho_0^*$ over time $t$ is shown in Figure 4. For all depicted ratios, a similar temporal evolution of the relative density is obtained. The relative density decreases (bone resorption) in the first loading step, $0 \leq t \leq 2$, and increases (bone formation) in all subsequent ones. On the right side of Figure 4, an additional enlarged view for $7 \leq t \leq 8$ is shown to visualize the differences of the resulting relative

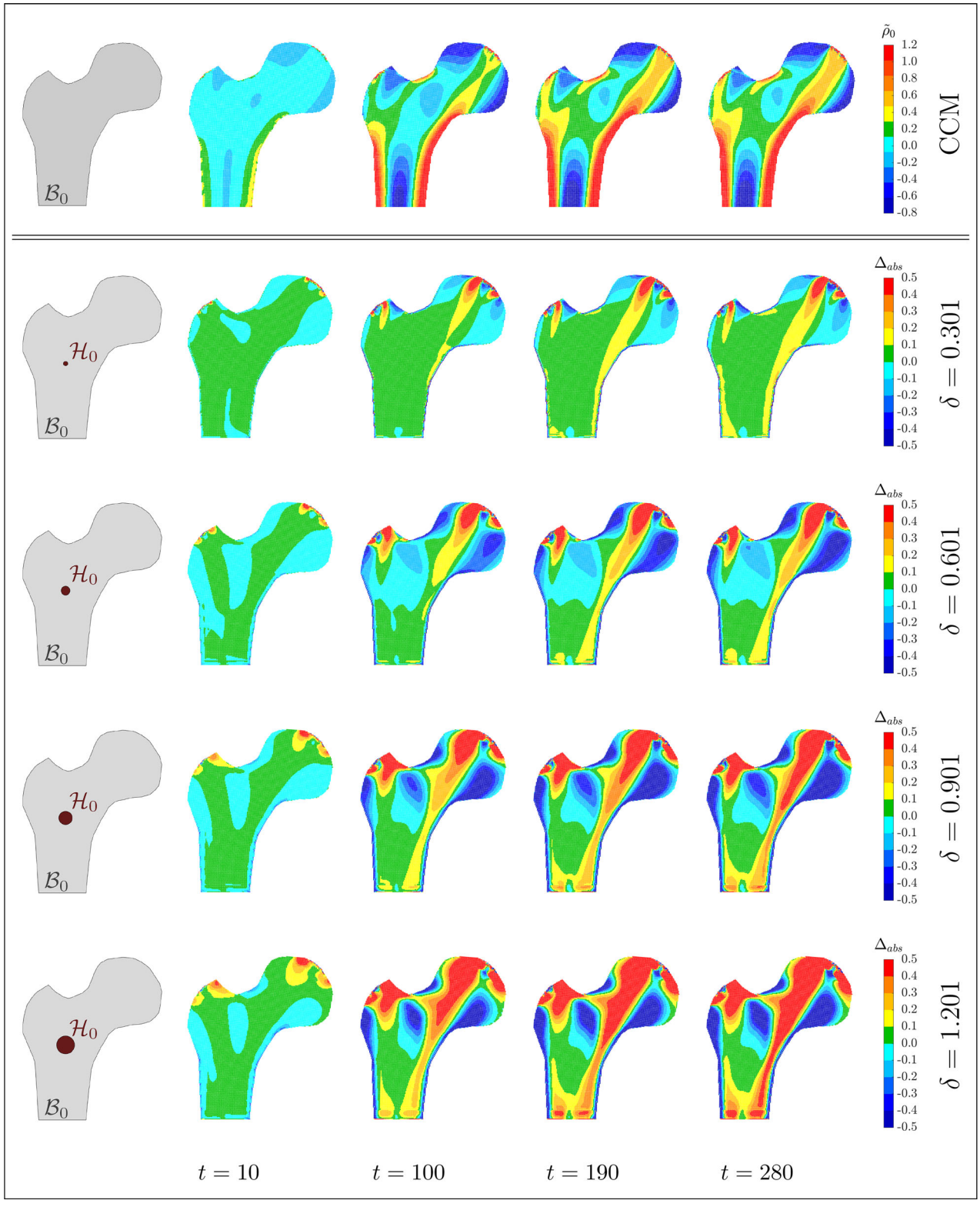


**Figure 10.** Distribution of the absolute change $\Delta_{\text{abs}} = \tilde{\rho}_{0_{\text{PD}}} - \tilde{\rho}_{0_{\text{CCM}}}$ for the simulations of the second load case. The resulting absolute change throughout the proximal femur is given for different time points $t = \{10,\ 100,\ 190,\ 280\}$ and horizon sizes $\delta = \{0.301,\ 0.601,\ 0.901,\ 1.201\}$ at fixed $\Delta = 0.1$. In the top row, the CCM results are given for comparison.

density evolution more clearly. As expected, the results converge with increasing number of neighbours within the horizon. The largest differences can be seen between the ratios $\delta/\Delta = 2.01$ and 2.5125. The differences between the larger ratios are no longer as significant compared to the smallest ratios that

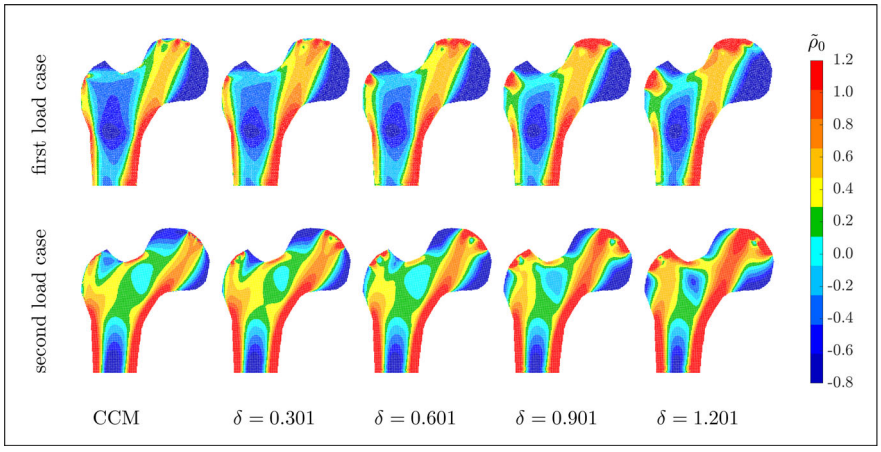


**Figure 11.** Comparison of resulting relative density distribution of the CCM and PD simulations at $t = 280$ for both load cases.

are depicted in Figure 4. The convergence study indicates to choose a sufficiently large ratio for an adequate number of integration points within $\mathcal{H}_0$.

Next, we study the influence of nonlocality by varying the horizon size $\delta$ with constant ratio $\delta/\Delta = 3.01$. The ratio $\delta/\Delta$ is fixed to have a constant number of integration points within the horizon for all simulations. We expect that the solution converges towards the CCM solution with diminishing horizon size. In Figure 5, the mean value over all material points of the relative density $\tilde{\rho}_0$ over time $t$ for $\delta = \{0.00940625,\ 0.0188125,\ 0.037625, 0.07525,\ 0.1505,\ 0.301\}$ is compared to the local solution with a St. Venant–Kirchhoff material model. As expected, the PD solution converges towards the local solution with decreasing horizon size. The remaining difference between the smallest horizon size and the local solution results from the slightly different energy densities used in the CCM and the PD model. Note that we need to make assumptions regarding the resulting deformation state in order to compute the peridynamic material parameter $C$ from the Young's modulus $E$ by comparing the two energy densities of Eqs. (13) and (23). The conversion of the material parameters $C$ and $E$ leads to a small error, which affects the modelled material stiffness and thus the density evolution. The deviation between the local and nonlocal solution additionally results from the disparities between the models regarding the application of boundary conditions and the so called surface effects. The latter describes the effect that *collocation points* at the surface do not have a full horizon. In terms of the unit square, surface effects mainly occur at the left and right edge. However, these surface effects are not a drawback of our nonlocal model, but rather a characteristic feature that are mentioned only as one of the reasons for the remaining small deviation from the local solution.

### 4.2. Proximal femur

The second example is motivated by the 2 D benchmark problem of the proximal femur, used in Carter and Beaupré (2000), Kuhl et al. (2003), Kuhl and Steinmann (2003), Papastavrou, Schmidt, Deng et al. (2020), Papastavrou, Schmidt and Steinmann (2020) and Schmidt et al. (2021). For the first load case, we combine the loading on the proximal femur that occurs due to various activities, as identified by Carter and Beaupré (2000). In accordance to Kuhl et al. (2003), Kuhl and Steinmann (2003), Papastavrou, Schmidt, Deng et al. (2020), Papastavrou, Schmidt and Steinmann (2020) and Schmidt et al. (2021), we apply the resulting forces of the combined loading on the proximal femur, as schematically depicted in Figure 6 (top left). Thereby, compressive forces on the femur head due to the contact with the pelvis and one tensile load on the greater trochanter, arising from the attached muscles, can be distinguished. As we restrict the presented PD formulation to Dirichlet boundary conditions, we first perform a force-controlled FEM simulation to obtain displacement values for the PD model. As depicted in Figure 6 (top right), we prescribe the obtained displacement values $\boldsymbol{u}_1$, $\boldsymbol{u}_2$, $\boldsymbol{u}_3$ and $\boldsymbol{u}_4$ directly at the loaded points $P_1$, $P_2$, $P_3$ and $P_4$ of the original benchmark problem.

The second load case, schematically illustrated in Figure 6 (bottom), is motivated by investigating the influence of the prescribed boundary conditions on the density evolution throughout the proximal femur. The boundary conditions are adopted from the load case used in Nackenhorst (1997). Here, a resulting tensile force $\boldsymbol{M}$ from the attached muscles acts on the greater trochanter and a resulting compressive force $\boldsymbol{J}$ from the hip joint on the femur head. Both forces are distributed among a small region, as indicated in Figure 6 (bottom left). The displacement values $\boldsymbol{u}_M$

and $\boldsymbol{u}_j$ obtained from a force-controlled FEM simulation are used to prescribe Dirichlet boundary conditions for the displacement-controlled simulations. In addition, we apply appropriate boundary conditions at the bottom edge to avoid rigid body motion in both load cases.

Initially, we assume a homogenous distribution of bone density with an initial density $\rho_0^* = 1.2$, as suggested in Kuhl and Steinmann (2003). The initial Young's modulus is uniformly set to $E = 500$, as in Carter and Beaupré (2000), Kuhl and Steinmann (2003), Papastavrou, Schmidt, Deng et al. (2020) and Papastavrou, Schmidt and Steinmann (2020). The peridynamic material parameter $C$ is computed according to the conversion of the energy densities in Eqs. (13) and (23), as mentioned in Section 4.1. We set $c = 1$, $\Psi_0^* = 0.01$, $n = 2$ and $m = 3$, as suggested in Kuhl and Steinmann (2003) and Papastavrou, Schmidt, Deng et al. (2020). The Poisson's ratio is typically set to $\nu = 0.2$ for cancellous bone, see Carter and Beaupré (2000). Regarding the presented PD model, we are however restricted to $\nu = 1/3$. We discretise the total simulation time $T = 280$ with an incremental time step of $\Delta t = 0.2$. The prescribed boundary conditions are applied linearly within the first 10 time increments.

For a structured spatial discretisation of the femur domain we use a grid spacing $\Delta = 0.1$, leading to 21,652 material (collocation) points for the PD model that additionally serve as discretisation nodes for the bi-linear elements of the FEM mesh. We examine the influence of nonlocality in the presented peridynamic formulation by increasing $\delta = \{0.301,\ 0.601,\ 0.901,\ 1.201\}$ while having a constant grid spacing $\Delta = 0.1$ that leads to a sufficiently fine mesh. We use a smallest ratio of $\delta/\Delta = 3.01$, for which we assume to obtain a sufficiently high accuracy of the integration over the horizon. Note that a ratio $\delta/\Delta \approx 3$ is commonly used in PD literature to minimise the computational effort while ensuring an adequate accuracy, see Silling and Askari (2005).

In the following, we first compare the resulting relative density distributions of the two load cases. In a second step, we evaluate the results with two radiographs of the proximal femur that can be found in Jacobs et al. (1995) and in Parkinson and Fazzalari (2013), respectively.

### Resulting density distributions of both load cases

An overview of the relative density distributions for the first load case is given in Figure 7 for four different time points $t = \{10,\ 100,\ 190,\ 280\}$. In the top row, the CCM results are added for comparison. In order to emphasise the differences between the CCM and PD results more clearly, the absolute change $\Delta_{\text{abs}} = \tilde{\rho}_{0_{\text{PD}}} - \tilde{\rho}_{0_{\text{CCM}}}$ is depicted in Figure 8. The corresponding results for the second load case are given in Figures 9 and 10, respectively. Note that the results are displayed at the *collocation points*.

For both load cases and for all horizon sizes $\delta$ we obtain the characteristic dense distribution evolving from the femur head and greater trochanter distally to the medial and lateral cortex due to the mechanical loading conditions, see Figures 7 and 9. It can be seen that the direction of loading and location of the mechanical boundary conditions determine the growth direction of the trabecular bone tissue. A loose density distribution in the intertrochanteric region occurs for the first load case and all horizon sizes. In contrast, for the second load case we obtain an increase in bone density in the intertrochanteric region, whereby a small region with slightly decreasing bone density evolves, observable by the bluish region in Figure 9. Comparing the results of the smallest horizon size $\delta = 0.301$ with the CCM results, we obtain mainly small absolute changes of $-0.1 \leq \Delta_{\text{abs}} \leq 0.1$ for both load cases, particularly for the earliest depicted time point $t = 10$, see Figures 8 and 10. The amount of absolute change slightly increases with time progressing, as indicated by the reddish and bluish regions of Figures 8 and 10. With increasing horizon size, equivalent to a more nonlocal material behaviour, we observe bigger differences with respect to the CCM results. Here, absolute changes of $|\Delta_{\text{abs}}| > 0.3$ occur, particularly at the greater trochanter and femur head. The bone formation and resorption is amplified near the Dirichlet boundary condition at the femur head with increasing horizon size for both load cases, compare Figures 7 and 9, respectively. Additionally, a significant difference between both load cases in terms of the resulting absolute changes can be identified, compare Figures 8 and 10.

Note that the results for $t = 10$ in Figures 7 and 8 show that the spherical increase in density at the boundary regions, both at the greater trochanter and femoral head, indicates the spherical shape of the horizon $\mathcal{H}_0$ used for the PD model.

### Comparison with radiographs of proximal femur from literature

We evaluate the resulting density distribution of the CCM and PD simulations by a comparison with two radiographs of the proximal femur that can be found in Jacobs et al. (1995) and in Parkinson and Fazzalari

(2013), respectively. To this end, we consider the evolving relative density distribution of both load cases at $t = 280$ of Figures 7 and 9 that are depicted together in Figure 11 for better comparison.

In both load cases, we obtain the dense distribution of cortical bone on the lateral and medial cortex for all horizon sizes. However, the increase in relative density is amplified at the lateral cortex for the second load case. Next, comparing the relative density distribution at the conjunction of the femoral neck and greater trochanter with the radiographs of Jacobs et al. (1995) and Parkinson and Fazzalari (2013), respectively, we receive better results with the second load case and particularly with increasing horizon size as the bone density increases in this region indicating the formation of cortical bone, see Figure 11. The relative density distribution in the intertrochanteric region is better captured by the second load case as all simulations replicate the secondary tensile and compressive group as well as the principle tensile group. In the first load case, on the other hand, the formation of the principle tensile group is apparent with increasing horizon size. The characteristic Ward's triangle, a region with lower bone density, is only captured by the simulations of the second load case, where we obtain a higher decrease in density for the more nonlocal PD simulations. However, the location of Ward's triangle is shifted laterally with increasing horizon size compared to the CCM result.

The second load case tends to overestimate the bone density distribution in the intertrochanteric region compared to the radiograph of Jacobs et al. (1995), but is in good accordance with the radiograph of Parkinson and Fazzalari (2013). The first load case, on the other hand, cannot replicate the dense trabecular bone distribution present in the intertrochanteric region of the radiograph published in Parkinson and Fazzalari (2013). Here, the simulation results are in better accordance with the radiograph of Jacobs et al. (1995), even though typical characteristics, such as Ward's triangle or the secondary compressive and tensile group, are not present in the CCM nor the PD simulations for the first load case.

The presented example of the proximal femur shows to what extent the additional degree of freedom, the nonlocality, in our PD model can influence the density distribution throughout the proximal femur.

## 5. Conclusions

In recent years, a variety of mathematical formulations have been proposed to describe the process of bone remodelling, where the classical continuum theory has served as the underlying framework for modelling bone as a continuum at the macro level. As an extension to the nonlinear local model of Kuhl and Steinmann (2003), we presented a nonlocal formulation for bone remodelling for the first time using PD.

We have performed two convergence studies on a unit square to validate our formulation. The first study has shown that the solution converges with increasing number of (collocation) points within the horizon. The second convergence study has demonstrated that with diminishing horizon size the PD solution converges towards the CCM solution. As a second numerical example, we simulated two load cases with a 2 D proximal femur model. Here, we have shown that the PD results with the smallest horizon size are in good accordance with the CCM results. With increasing horizon size the relative density distribution obtained by the CCM simulation and thus characteristic for the applied load case remains, where in the first load case the formation of the principle tensile group is indicated with increasing horizon size as outlined by a comparison of all simulation results and two radiographs of the proximal femur from literature. For the second load case, the formation of cortical bone at the greater trochanter and femur neck is better captured with the more nonlocal PD simulations. A comparison of the two load cases regarding both the CCM and PD results highlighted the significant influence of the applied mechanical boundary conditions. Comparing the resulting relative density distributions with two radiographs from literature additionally showed that the second load case better replicates the main characteristics of the density distribution throughout the proximal femur and emphasised the importance of patient-specific simulations and evaluation of results. Note that an investigation regarding the load case and applied mechanical boundary conditions on the proximal femur are not within the scope of this contribution. Nevertheless, an extensive study on the load case and resulting density distribution shall be of interest in future research. For this, the local continuum model for bone remodelling is sufficient as the CCM and PD simulations resulted in a relative density distribution characteristic for the load case. In this contribution, however, we focused on demonstrating the influence of nonlocality on the relative density distribution of our PD model and therefore limited ourselves to the two presented load cases.

In summary, the presented nonlocal formulation enables to model and investigate nonlocal material

behaviour during bone remodelling by varying the horizon size. Reasonable results were obtained in both numerical examples for all presented horizon sizes. In this contribution, we focused on illustrating the main aspects of the peridynamic formulation with two numerical examples. In future research, the nonlocal characteristic of bone remodelling shall be further examined while applying more realistic loading conditions and material behaviour in order to fully capture the density distribution of the proximal femur.

## Disclosure statement

The authors declare that they have no conflict of interest.

## Funding

Ali Javili gratefully acknowledges the support provided by the Scientific and Technological Research Council of Turkey (TÜBITAK) Career Development Program, grant number 218M700.

## ORCID

E. Schaller http://orcid.org/0000-0003-0497-3398
A. Javili http://orcid.org/0000-0001-7965-7088
A. Papastavrou http://orcid.org/0000-0002-4541-6208
P. Steinmann http://orcid.org/0000-0003-1490-947X

## References

Buganza Tepole A, Kuhl E. 2016. Computational modeling of chemo-bio-mechanical coupling: a systems-biology approach toward wound healing. Comput Methods Biomech Biomed Eng. 19(1):13–30.

Carter DR, Beaupré GS. 2000. Skeletal function and form: mechanobiology of skeletal development, aging, and regeneration. New York (NY): Cambridge University Press.

Carter DR, Hayes WC. 1977. The behavior of bone as a two-phase porous structure. J. Bone Joint Surg. 59-A:785–794.

Cowin SC, Hegedus DH. 1976. Bone remodeling I: theory of adaptive elasticity. J Elasticity. 6(3):313–326.

Della Corte A, Giorgio I, Scerrato D. 2020. A review of recent developments in mathematical modeling of bone remodeling. Proc Inst Mech Eng H. 234(3):273–281.

Deng Q, Chen Y, Lee JD. 2009. An investigation of the microscopic mechanism of fracture and healing processes in cortical bone. Int J Damage Mech. 18(5):491–502.

Frost HM. 1987. Bone "mass" and the "mechanostat": a proposal. Anat Rec. 219(1):1–9.

George D, Allena R, Remond Y. 2018. A multiphysics stimulus for continuum mechanics bone remodeling. Math Mech Compl Sys. 6(4):307–319.

Ghajari M, Iannucci L, Curtis P. 2014. A peridynamic material model for the analysis of dynamic crack propagation in orthotropic media. Comput Methods Appl Mech Eng. 276:431–452.

Gibson LJ, Ashby MF. 1982. The mechanics of three-dimensional cellular materials. Proc R Soc Lond. A. Math Phys Sci. 382(1782):43–59.

Gibson LJ. 2005. Biomechanics of cellular solids. J Biomech. 38(3):377–399.

Giorgio I, dell'Isola F, Andreaus U, Alzahrani F, Hayat T, Lekszycki T. 2019. On mechanically driven biological stimulus for bone remodeling as a diffusive phenomenon. Biomech Model Mechanobiol. 18(6):1639–1663.

Harrigan TP, Hamilton JJ. 1993. Finite element simulation of adaptive bone remodelling: a stability criterion and a time stepping method. Int J Numer Methods Eng. 36(5):837–854.

Harrigan TP, Hamilton JJ. 1994. Necessary and sufficient conditions for global stability and uniqueness in finite element simulations of adaptive bone remodeling. Int J Solids Struct. 31(1):97–107.

Jacobs CR, Levenston ME, Beaupré GS, Simo JC, Carter DR. 1995. Numerical instabilities in bone remodeling simulations: the advantages of a node-based finite element approach. J Biomech. 28(4):449–459.

Javili A, Firooz S, McBride AT, Steinmann P. 2020. The computational framework for continuum-kinematics-inspired peridynamics. Comput Mech. 66(4):795–824.

Javili A, McBride AT, Steinmann P. 2019. Continuum-kinematics-inspired peridynamics. Mechanical problems. J Mech Phys Solids. 131:125–146.

Javili A, Morasata R, Oterkus E, Oterkus S. 2019. Peridynamics review. Math Mech Solids. 24(11):3714–3739.

Kuhl E, Steinmann P. 2003. Theory and numerics of geometrically non-linear open system mechanics. Int J Numer Methods Eng. 58 (11):1593–1615.

Kuhl E, Menzel A, Steinmann P. 2003. Computational modeling of growth - a critical review, a classification of concepts and two new consistent approaches. Comput Mech. 32(1-2):71–88.

Kumar C, Jasiuk I, Dantzig J. 2011. Dissipation energy as a stimulus for cortical bone adaptation. J Mech Mater Struct. 6(1–4):303–319.

Martin RB, Burr DB, Sharkey NA, Fyhrie DP. 1998. Skeletal tissue mechanics. Vol. 190. New York (NY): Springer.

Nackenhorst U. 1997. Numerical simulation of stress stimulated bone remodeling. Tech Mech. 17(1):31–40.

Papastavrou A, Schmidt I, Deng K, Steinmann P. 2020. On age-dependent bone remodeling. J Biomech. 103:109701.

Papastavrou A, Schmidt I, Steinmann P. 2020. On biological availability dependent bone remodeling. Comput Methods Biomech Biomed Engin. 23(8):432–444.

Parkinson IH, Fazzalari NL. 2013. Characterisation of trabecular bone structure. In: Skeletal aging and osteoporosis. Berlin, Heidelberg: Springer; p. 31–51.

Schmidt I, Albert J, Ritthaler M, Papastavrou A, Steinmann P. 2021. Concurrent consideration of cortical and cancellous bone within continuum bone remodelling. Comput Methods Biomech Biomed Eng. :1–12.

Silling SA. 2000. Reformulation of elasticity theory for discontinuities and long-range forces. J Mech Phys Solids. 48 (1):175–209.

Silling SA, Askari E. 2005. A meshfree method based on the peridynamic model of solid mechanics. Comput Struct. 83(17–18):1526–1535.

Wolff J. 1892. Das Gesetz der Knochentransformation. Berlin: Hirschwald.

## Appendix A. Stiffness matrices for biomechanically coupled bone remodelling problem

The stiffness matrices ${}^{\rho\rho}\mathbb{K}^{ab}$ and ${}^{\rho\boldsymbol{x}}\mathbb{K}^{ab}$ of the linearisation of the residual ${}^{\rho}\mathbb{R}^{a}$ (21) are computed by

$$ {}^{\rho\rho}\mathbb{K}^{ab} = \frac{\partial^{\rho}\mathbb{R}^{a}}{\partial\rho_b} = -1 + c\left[\frac{\rho_0^a}{\rho_0^*}\right]^{-m}\frac{1}{2}\sum_{\substack{i=1\\ i\neq a}}^{\mathcal{N}}\left[\frac{-m}{\rho_0^a} + \frac{n}{\hat{\rho}_{0_i}^{\downarrow}}\frac{\partial\hat{\rho}_{0_i}^{\downarrow}}{\partial\rho_b}\right]\left[\frac{\hat{\rho}_{0_i}^{\downarrow}}{\rho_0^*}\right]^{n}\psi_{0_i}^{\downarrow\mathrm{PD}}V_i^{\downarrow}\Delta t. \tag{A1}$$

and

$$ {}^{\rho\boldsymbol{x}}\mathbb{K}^{ab} = \frac{\partial^{\rho}\mathbb{R}^{a}}{\partial x_b} = c\left[\frac{\rho_0^a}{\rho_0^*}\right]^{-m}\frac{1}{2}\sum_{\substack{i=1\\ i\neq a}}^{\mathcal{N}}\left[\frac{\hat{\rho}_{0_i}^{\downarrow}}{\rho_0^*}\right]^{n}C\left[\frac{1}{|\boldsymbol{\Xi}_i^{\downarrow}|} - \frac{1}{|\boldsymbol{\xi}_i^{\downarrow}|}\right]\boldsymbol{\xi}_i^{\downarrow}\frac{\partial\boldsymbol{\xi}_i^{\downarrow}}{\partial\mathbb{X}_b}V_i^{\downarrow}\Delta t, \tag{A2}$$

where we omit the subscript $n+1$ for better readability as the tangents only depend on quantities of $t_{n+1}$. The partial derivatives

$$ \frac{\partial\hat{\rho}_{0_i}^{\downarrow}}{\partial\rho_b} = \frac{1}{2}[\delta^{ab} + \delta^{ib}] \qquad \text{and} \qquad \frac{\partial\boldsymbol{\xi}_i^{\downarrow}}{\partial\mathbb{X}_b} = [\delta^{ib} - \delta^{ab}], \tag{A3}$$

are given in terms of the Kronecker delta

$$ \delta^{ij} = \begin{cases} 1 & i = j \\ 0 & i \neq j \end{cases}. $$

The stiffness matrices ${}^{\boldsymbol{x}\rho}\mathbb{K}^{ab}$ and ${}^{\boldsymbol{x}\boldsymbol{x}}\mathbb{K}^{ab}$ of the linearisation of ${}^{\boldsymbol{x}}\mathbb{R}^{a}$ (22) read

$$ {}^{\boldsymbol{x}\rho}\mathbb{K}^{ab} = \frac{\partial^{\boldsymbol{x}}\mathbb{R}^{a}}{\partial\rho_b} = \sum_{\substack{i=1\\ i\neq a}}^{\mathcal{N}}\left[\frac{\hat{\rho}_{0_i}^{\downarrow}}{\rho_0^*}\right]^{n}\frac{n}{\hat{\rho}_{0_i}^{\downarrow}}\frac{\partial\hat{\rho}_{0_i}^{\downarrow}}{\partial\rho_b}C\left[\frac{1}{|\boldsymbol{\Xi}_i^{\downarrow}|} - \frac{1}{|\boldsymbol{\xi}_i^{\downarrow}|}\right]\boldsymbol{\xi}_i^{\downarrow}V_i^{\downarrow}, \tag{A4}$$

and

$$ {}^{\boldsymbol{x}\boldsymbol{x}}\mathbb{K}^{ab} = \frac{\partial^{\boldsymbol{x}}\mathbb{R}^{a}}{\partial x_b} = \sum{}_{\substack{i=1\\ i\neq a}}^{\mathcal{N}}\left[\frac{\hat{\rho}_{0_i}^{\downarrow}}{\rho_0^*}\right]^{n}C\left[\frac{1}{|\boldsymbol{\xi}_i^{\downarrow}|^3}\boldsymbol{\xi}_i^{\downarrow}\otimes\boldsymbol{\xi}_i^{\downarrow} + \left[\frac{1}{|\boldsymbol{\Xi}_i^{\downarrow}|} - \frac{1}{|\boldsymbol{\xi}_i^{\downarrow}|}\right]\mathbf{1}\right]\frac{\partial\boldsymbol{\xi}_i^{\downarrow}}{\partial\mathbb{X}_b}V_i^{\downarrow}. \tag{A5}$$